PHYSICAL REVIEW RESEARCH **5**, 033159 (2023)

Pulse variational quantum eigensolver on cross-resonance-based hardware

Daniel J. Egger[1,*] Chiara Capecci[2] Bibek Pokharel[3] Panagiotis Kl. Barkoutsos[1,†] Laurin E. Fischer[1,4]
Leonardo Guidoni[5] and Ivano Tavernelli[1]
[1]*IBM Quantum – IBM Research Europe - Zurich, Säumerstrasse 4, 8803 Rüschlikon, Switzerland*
[2]*Dipartimento di Ingegneria e Scienze dell'Informazione e Matematica, Università degli Studi dell'Aquila, 67100 Coppito, L'Aquila, Italy*
[3]*IBM Quantum – IBM Research Almaden, 650 Harry Road, San Jose, California 95120, USA*
[4]*Theory and Simulation of Materials (THEOS), École Polytechnique Fédérale de Lausanne, 1015 Lausanne, Switzerland*
[5]*Dipartimento di Scienze Fisiche e Chimiche, Università degli Studi dell'Aquila, 67100 Coppito, L'Aquila, Italy*

(Received 17 April 2023; accepted 8 August 2023; published 5 September 2023)

State-of-the-art noisy digital quantum computers can only execute short-depth quantum circuits. Variational algorithms are a promising route to unlock the potential of noisy quantum computers since the depth of the corresponding circuits can be kept well below hardware-imposed limits. Typically, the variational parameters correspond to virtual R_Z gate angles, implemented by phase changes of calibrated pulses. By encoding the variational parameters directly as hardware pulse amplitudes and durations, we succeed in further shortening the pulse schedule and overall circuit duration. This decreases the impact of qubit decoherence and gate noise. As a demonstration, we apply our pulse-based variational algorithm to the calculation of the ground state of different hydrogen-based systems (H_2, H_3, and H_4) using IBM cross-resonance-based hardware. We observe a reduction in schedule duration of up to 5× compared to CNOT-based *Ansätze*, while also reducing the measured energy. In particular, we observe a sizable improvement of the minimal energy configuration of H_3 compared to a CNOT-based variational form. Finally, we discuss possible future developments including error-mitigation schemes and schedule optimizations, which will enable further improvements of our approach, paving the way towards the simulation of larger systems on noisy quantum devices.

DOI: 10.1103/PhysRevResearch.5.033159

I. INTRODUCTION

Current quantum computers are noisy and are constituted of qubits with finite coherence times. This bounds the depth of the circuits that they can reliably execute. There is thus a large interest in short-depth noise-resilient algorithms such as the variational quantum algorithm (VQA) [1]. VQAs can be applied to quantum chemistry [2–6], machine-learning [7–9], and optimization [10] tasks. In a VQA, the expectation value $\langle\psi(\boldsymbol{\theta})|\mathcal{O}|\psi(\boldsymbol{\theta})\rangle$ of an observable $\mathcal{O}$ is optimized by varying the parameters $\boldsymbol{\theta}$ of a trial variational state $|\psi(\boldsymbol{\theta})\rangle$. Typically, the variational state is prepared by a parameterized quantum circuit, the *Ansatz*. For example, in quantum chemistry, $|\psi(\boldsymbol{\theta})\rangle$ can be prepared with the unitary coupled cluster with singles and doubles (UCCSD) *Ansatz* [11]. For combinatorial optimization, the quantum approximate optimization algorithm prepares a trial state by alternating applications of a cost-function operator and a mixer operator [12–15]. However, many *Ansätze* are often still too deep for execution on current quantum hardware [11,16]. This has spurred an interest to generate variational states with more resource-efficient circuits [17–21]. In superconducting qubits [22–24], the circuit instructions are translated into microwave pulses that manipulate the quantum information. For example, on IBM Quantum systems, all circuits are broken down into the hardware-native basis gates $\{X, \sqrt{X}, \text{CNOT}, R_Z(\theta)\}$. Here, the X, $\sqrt{X}$, and CNOT gates are implemented by carefully calibrated pulses. All the parameters of a circuit are therefore encoded in the virtual-Z rotations $R_Z(\theta)$, i.e., zero-duration instructions that only change the phase of subsequent pulses [25]. The duration of the *Ansatz* is thus independent of the optimization parameters $\boldsymbol{\theta}$.

The pulses implementing the native basis gate set are carefully calibrated *a priori*, a costly task typically done with error-amplifying gate sequences [26] and sometimes optimal control [27]. Quantum optimal control (OC) has a long history [28–30] and provides methods to create quantum states [31,32] and gates [33–35], and control nonunitary dynamics [36] such as a measurement process [37,38]. However, in superconducting qubits, model inaccuracies make it difficult to apply pulses generated through simulations [39]. One must either improve the model [40] or resort to closed-loop optimal control on the hardware [39]. In closed-loop optimal control, a cost function, which can correspond to a gate fidelity, is optimized by an algorithm that varies parameters in a parameterized pulse shape [27,34]. Similarly, in a VQA, the expectation value of an observable is optimized by varying

---

[*] deg@zurich.ibm.com

[†] Presently at PASQAL.

parameters in a parameterized quantum circuit which is ultimately lowered to pulses. Closed-loop optimal control and VQAs can thus be viewed as the same task [41].

Currently, VQAs with the basis gate set $\{X, \sqrt{X}, \text{CNOT}, R_Z(\theta)\}$ amount to optimizing phases, while OC optimizes pulse parameters. Pulse-level control of cloud-based quantum computers [42,43] enables a direct optimization of the pulse parameters in the variational quantum eigensolver (VQE) [44]. This has been explored in previous works, which we briefly summarize. The authors of Ref. [45] show how to optimize only the amplitude of pulses on cross-resonance (CR) systems [46] to increase the accuracy of a binary classification. On the other hand the authors of Ref. [47] let the variational algorithm change the amplitude and frequency of the pulses. However, optimizing only pulse amplitudes and not durations makes it impossible to mitigate decoherence by adaptively shortening the pulse schedule. Indeed, this is what has been proposed in Ctrl-VQE, where both the duration and the amplitude of square pulses is optimized [48]. Numerical simulations show that leakage outside of the computational space can reduce the state preparation time in Ctrl-VQE and improve results [49]. Finally, in Ref. [50], the authors study a pulse-based variational *Ansatz* in which the duration of two-qubit CR gates is optimized at a fixed amplitude. They show numerical simulations that achieve chemical accuracy on molecules that require up to four qubits and present hardware results for H_2 on two qubits.

In this work, we simultaneously optimize single-qubit pulses as well as both the duration and the amplitude of the CR pulses. Here we demonstrate a pulse-based VQE that optimizes both duration and amplitude with systems that use up to eight qubits. Furthermore, we perform the full VQE parameter optimization on quantum hardware. This allows the optimizer to capture T_1- and T_2-related tradeoffs that favor short and intense pulses. For context, the largest VQE by qubit count on hardware was done on 20 qubits with parameters optimized in a noiseless simulation [6]. In addition, we discuss the implementation of advanced error mitigation in pulse-based VQAs, which is tricky since the effect of the pulses is hard to capture.

In Sec. II, we review the dynamics of the CR gate and existing connections to variational algorithms. In Sec. III, we introduce the chemical systems that we study, namely, H_2, H_3, and H_4. Next, in Sec. IV, we study these systems on devices with up to eight qubits. We discuss error mitigation in Sec. V and conclude in Sec. VI.

II. CROSS-RESONANCE DYNAMICS AND VARIATIONAL QUANTUM ALGORITHMS

Dispersively coupled fixed-frequency transmon qubits can be entangled with the CR interaction [46,51,52]. Here, one qubit, i.e., the control, is driven at the frequency of the other, i.e., the target. The resulting effective Hamiltonian is

$$\bar{H}_{cr} = \tfrac{1}{2}(Z \otimes B + I \otimes C), \tag{1}$$

where $B = \omega_{ZI} I + \omega_{ZX} X + \omega_{ZY} Y + \omega_{ZZ} Z$ and $C = \omega_{IX} X + \omega_{IY} Y + \omega_{IZ} Z$. Here, X, Y, and Z are Pauli matrices and I is the identity. The coefficients ω_{ij} are the strength of the CR interaction. They depend on the properties of the qubits and the drive strength [53]. To illustrate the dynamics of the cross-resonance gate, we first measure the ω_{ij}'s with Hamiltonian tomography [46] implemented in QISKIT EXPERIMENTS. Next, we simulate Eq. (1) with QISKIT DYNAMICS. The strongest terms in $\bar{H}_{cr}$ are ω_{ZX} and ω_{IX}; see Fig. 1. The CR interaction is typically used to engineer a CNOT gate by eliminating the non-ZX terms with an echo sequence and cancellation tones [54]. The phase of the CR drive controls the relative magnitude of the ω_{ZX} and ω_{ZY} coefficients. Simulations of the time evolution under $\bar{H}_{cr}$ and Hamiltonian tomography show that the echo cancels the large ω_{IX} term; see Fig. 1. With or without an echo, the resulting entanglement is usable in VQAs by replacing CNOT gates by CR tones with fixed parameters, as done in Ref. [55]. Here, the resulting *Ansätze* are parameterized by virtual-Z rotations.

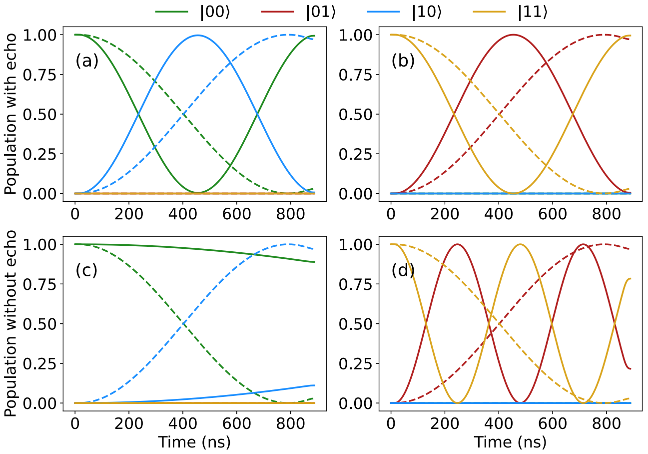

FIG. 1. Dynamics of the cross-resonance gate. The states are labeled according to |target, control⟩. The simulation is done (a), (b) with an echo and (c), (d) without an echo. In both cases, the strength of the ω_{ij} in Eq. (1) is measured on qubits (0, 1) of *ibm_lagos* with Hamiltonian tomography [57]. The strength of the cross-resonance terms without an echo is reported in Appendix E. With an echo, we measure $\omega_{ZX} = 872(2)$ kHz, $\omega_{ZY} = 715(2)$ kHz, $\omega_{ZZ} = -35(1)$ kHz, $\omega_{IX} = 53(1)$ kHz, $\omega_{IY} = -69(2)$ kHz, and $\omega_{IZ} = -35(1)$ kHz. The dashed line shows the population when only the ZX term is retained.

The ω_{ij}'s are nonlinear with drive amplitude [53], but the rotation implemented by $\exp(-i\tau\bar{H}_{cr})$ is linear in time τ. The linearity in τ enables transpiler passes to create $R_{ZX}(\theta)$ rotations built from calibrated CNOT gates by scaling the duration of cross-resonance pulses [56]. The resulting shorter pulses reduce hardware errors in quantum approximate optimization [16,56] and machine learning [9], which are both a form of pulse-based VQA.

III. TEST SYSTEMS: APPLICATIONS TO QUANTUM CHEMISTRY

In this work, we investigate pulse-based VQE on hydrogen-based systems. We consider molecular hydrogen H_2, the triangular H_3, and the rectangular H_4 [58]; see Fig. 2. The triangular H_3 is highly frustrated and the rectangular H_4 has strong correlations, making both systems interesting to study. We model all the systems in the minimal Gaussian basis set Slater-type orbital (STO)-3G. The fermionic problem is

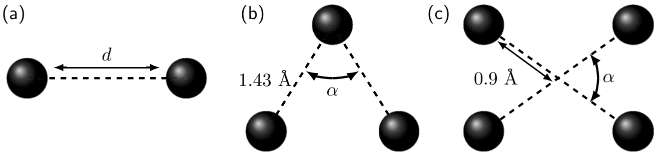

FIG. 2. Considered hydrogen-based systems. (a) For H_2, we vary the distance d. (b) For H_3, we vary the angle α, and (c) for H_4, we consider the angle $\alpha = 40^\circ$.

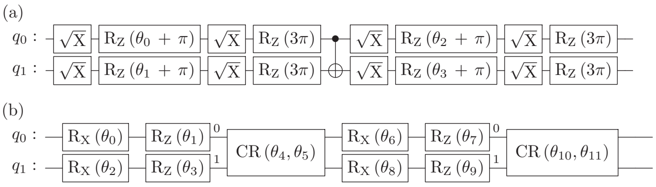

FIG. 3. H_2 *Ansätze*. (a) In the CNOT-based variational form, there are four parameters in virtual-Z gates. (b) In the pulse-based variational form, there are 12 parameters.

mapped to a Hamiltonian expressed as the linear combination, $H = \sum_i \alpha_i P_i$. Here, the α_i's are coefficients and the P_i's are Pauli operators made of tensor products of single-qubit Pauli matrices I, X, Y, and Z, e.g., $YZYXXI$. A parameterized circuit *Ansatz* creates a state $|\psi(\boldsymbol{\theta})\rangle$ on the quantum hardware. As a cost function, we minimize the energy, i.e., $\min_{\boldsymbol{\theta}} \langle\psi(\boldsymbol{\theta})|H|\psi(\boldsymbol{\theta})\rangle$, in a closed loop with the hardware. To reduce the number of quantum circuits to measure, we group the Pauli operators $\{P_i\}$ into qubitwise commuting groups. This allows us to measure each group with a single basis change before the final measurement.

In the STO-3G basis, each hydrogen atom requires two qubits to model, i.e., one for each spin orbital. H_2, the exception, is mapped to spin operators with the parity mapping [59] and a reduction to two qubits, leveraging particle number conservation, resulting in five Pauli terms. The H_2 dissociation curve is often studied as a benchmark for VQAs [2,17,50,60]. H_3 has a triangular geometry and we map this fermionic system to six qubits with the Jordan-Wigner transformation. The resulting 62 Pauli terms are measured in 21 sets of qubitwise commuting elements. Initially, we compute the dissociation curve for the equilateral system using the classical full configuration interaction (full CI) method to find the bond distance. We then study the dissociation curve of a more general isosceles conformation with two equal sides of the triangle fixed at the 1.43 Å bonding distance of the equilateral H_3. Here, we vary the angle α between the two sides; see Fig. 2(b). We map the rectangular H_4 system to eight qubits with the Jordan-Wigner transformation. The resulting 97 Pauli terms are measured in 35 sets of qubitwise commuting elements. We first find the bond distance of the square system by computing the dissociation curve with full CI. The square H_4 at the 0.9 Å equilibrium distance serves as a starting point to study a rectangular H_4 system with an angle $\alpha = 40^\circ$ between the two 1.8 Å fixed-length diagonals; see Fig. 2(c). In general, the number of required qubits increases with the number of atoms and size of the spin orbital basis set. By considering only the chemically active orbitals of a molecule, e.g., with an embedding scheme [61,62], the number of required qubits can be reduced, which helps implement VQE on noisy quantum hardware [11].

IV. PULSE-BASED VQA FOR HYDROGEN-BASED SYSTEMS

We now study H_2, H_3, and H_4 as described in Sec. III on IBM Quantum cross-resonance-based hardware. We compare CNOT-based and pulse-based *Ansätze*, which match the qubit connectivity. The CNOT-based *Ansatz* is built from the REALAMPLITUDE blueprint circuit in QISKIT [63] consisting of CNOT gates sandwiched by $R_Y(\theta)$ rotations, here decomposed to $\sqrt{X}$ and $R_Z(\theta)$ gates.

The pulse level allows an arbitrary parametrization of the controls. In the extreme case, each sample of the arbitrary waveform generator is a control parameter to optimize. This enables extremely short single-qubit gates without leakage, but results in an optimization landscape with many parameters [27]. To make a control scheme practical, the number of parameters to optimize must be kept reasonable [64]. We therefore employ pulse-based *Ansätze* in which each single-qubit gate is a derivative removal by adiabatic gate (DRAG) pulse [65], indicated by $R_X(\theta)$, with an amplitude controlled by the optimizer. This avoids the double $\sqrt{X}$ decomposition, shown in Fig. 3(a), sparing one pulse. The duration, standard deviation, and DRAG parameter are obtained from the calibrated X gate of the backend. Entanglement is created by cross-resonance tones, each implemented as a single GaussianSquare pulse, i.e., a flat-top pulse with Gaussian edges, applied to the control qubit (0) at the frequency of the target qubit (1). The standard deviation σ of the flanks is $64\,dt$ with each flank containing 2σ. The duration of a single sample of the arbitrary waveform generator is $dt = 0.222$ ns. By contrast with Ref. [50], both the amplitude and duration of the CR pulses are variational parameters and we do not introduce an echo in the CR tones to keep them short. Crucially, the hardware only accepts pulses with a duration that is a multiple of 16 samples and an amplitude ranging from -1 to 1. To satisfy these conditions, we introduce parameter wrapping functions, described in Appendix B. Any nonlinearity resulting from changes in the pulse amplitude is dealt with by the optimizer.

A. Hydrogen molecule

We first run a VQE to find the ground state of H_2 on *ibm_lagos* on qubits 0 and 1. We compare the circuit-based *Ansatz* in Fig. 3(a) to the pulse-based variational form in Fig. 3(b) in their ability to approach the exact full CI energy obtained in the chosen STO-3G molecular basis. Simulations indicate that at least two CR pulses are needed for the pulse-based *Ansatz* to converge; see Appendix A. Since the amplitude in the CR pulse is a real parameter, we add a virtual-Z gate before each CR gate to control the phase of the cross-resonance drive.

The optimization is done with constrained optimization by linear approximation (COBYLA) with 4096 shots per circuit. Both the CNOT- and the pulse-based *Ansätze* closely reproduce the energy; see Fig. 4. These results do not make use of readout-error mitigation (REM) and are

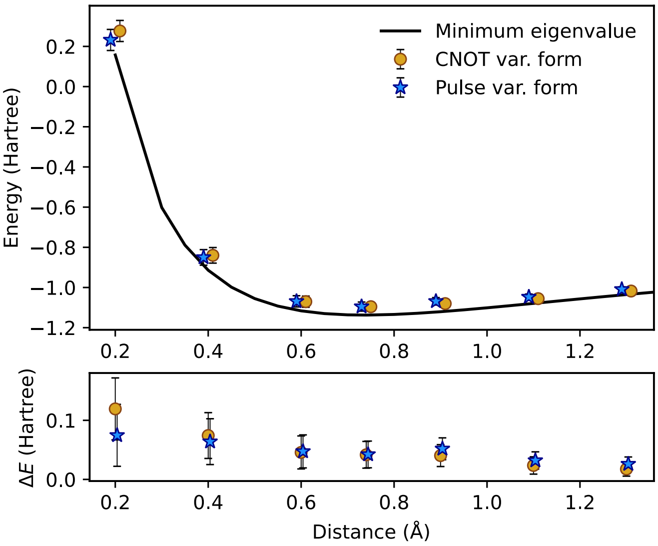

FIG. 4. Energy in H_2. The golden dots show the CNOT-based *Ansatz*. The blue stars show the pulse-based *Ansatz*. The black line is the exact energy. The bottom panel shows the energy difference ΔE between VQE and the exact diagonalization. The error bars show an upper bound on the sampling error of the estimator; see Appendix C. They are increased by a factor of two and markers are slightly x-shifted for visibility purposes.

comparable to the non-readout-error-mitigated results in Ref. [50]. The duration of our CNOT-based variational form, shown in Fig. 5, is 3360 dt and the duration of the pulse-based *Ansatz* is 928 ± 114 dt averaged over the considered distances d. This corresponds to a difference in duration of 0.54 µs since $dt = 0.222$ ns. We do not expect the pulse-based *Ansatz* to produce a significant gain over the CNOT-based one. Indeed, (i) the noiseless CNOT-based *Ansatz* exactly creates the ground state of H_2, (ii) the 0.54 µs schedule difference is small compared to the T_1 and T_2 times shown in Appendix E, and (iii) the results are dominated by readout errors. Overall, even in this simple example, pulse-based VQE delivers a shorter schedule than a CNOT-based VQE without affecting performance. The next two sections show that this trend generalizes: the shorter pulse-based VQE schedules outperform their CNOT counterparts.

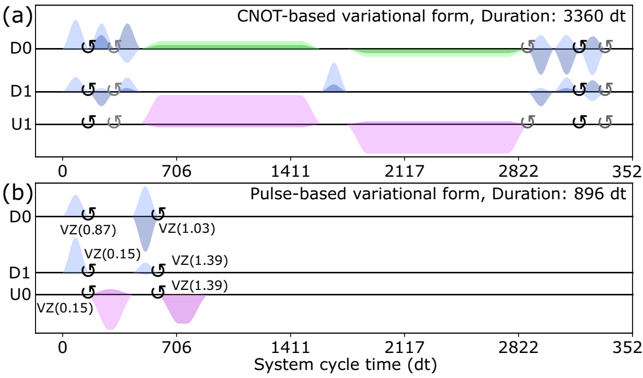

FIG. 5. Optimized pulse schedules for H_2 at 0.2 Å. (a) CNOT-based and (b) pulse-based *Ansätze*. The circular arrows indicate zero-duration virtual-Z (VZ) gates. In the CNOT-based *Ansatz*, the black virtual-Z gates are the only parameterized instructions. The drive channels Di indicate single-qubit pulses on qubit i and the control channels Uj indicate cross-resonance tones; see details in Appendix E.

B. Three hydrogen atoms

The H_3 system is larger than the H_2 molecule; it requires a total of six qubits. We search for the ground state of H_3 as a function of the angle α on *ibm_lagos* with qubits 0–5. A direct diagonalization of H_3 reveals a ground state with only real amplitudes at all considered angles. We therefore compare a CNOT-based REALAMPLITUDE *Ansatz*, shown in Fig. 6(a), to a pulse-based one with the same structure, shown in Fig. 6(b). In both circuits, the ladder of two-qubit gates matches the qubit connectivity of *ibm_lagos*; see Appendix E. For H_3, we focus on the depth-one CNOT-based variational form, which has 12 parameters, since deeper *Ansätze* did not improve the energy; see Appendix D. The pulse-based variational form has a total of 22 optimization parameters: 12 single-qubit pulse amplitudes, 5 CR durations, and 5 CR amplitudes. As with H_2, we use COBYLA with 4096 shots per circuit evaluation.

We first find the electronic energy for the angle $\alpha = 20^\circ$ starting from a random guess for the variational parameters θ. We then find the electronic energy in increments of 2° by initializing the optimization from the best parameters of the previous angle α. Next, we compute the energy by adding the repulsion energy to the VQE-computed electronic energy. The resulting energy of the pulse-based *Ansatz* is $33.0 \pm 7.8\%$ closer, averaged over all angles, to the ideal minimum energy than the CNOT-based one; see Fig. 7. Note that the phases of the CR gates were not optimized. To find the angle α_{min} that minimizes the energy of H_3, we fit the measured energy to fourth-order polynomials, shown as dashed lines in Fig. 7. The pulse-based and CNOT-based approaches report an α_{min} of 30.1° and 36.4°, respectively. Full CI yields an α_{min} of 29.3°; the pulse-based results are therefore more accurate than the CNOT-based ones.

We repeat these measurements with readout-error mitigation implemented using the tensored measurement fitter in QISKIT. Here, each CNOT-based and pulse-based VQE run is initialized with the optimal parameters found without readout-error mitigation for the corresponding *Ansatz* and angle α. REM significantly reduces the errors; e.g., compare the blue stars to the blue triangles in Fig. 7(a). With REM, the pulse-based and CNOT-based VQE report an α_{min} of 27.7° and 38.2°, respectively. Furthermore, with REM, the pulse-based VQE has a $52 \pm 16\%$ lower error with respect to the full CI computation than the CNOT-based *Ansatz*. Interestingly, we observe that REM lowered the absolute difference between the VQE and the full CI energy. However, it increased the deviation of α_{min} with respect to the ideal 29.3° value as the fourth-order polynomial overfits the data.

The pulse-based *Ansatz* has more parameters than its CNOT counterpart, which may increase its expressivity. However, the pulse-based VQE schedule is simpler than the CNOT one; see Fig. 8. For example, the pulse-based *Ansatz* only has 12 single-qubit DRAG pulses. By contrast, the CNOT-based schedule has 45 single-qubit DRAG pulses to decompose R_Y

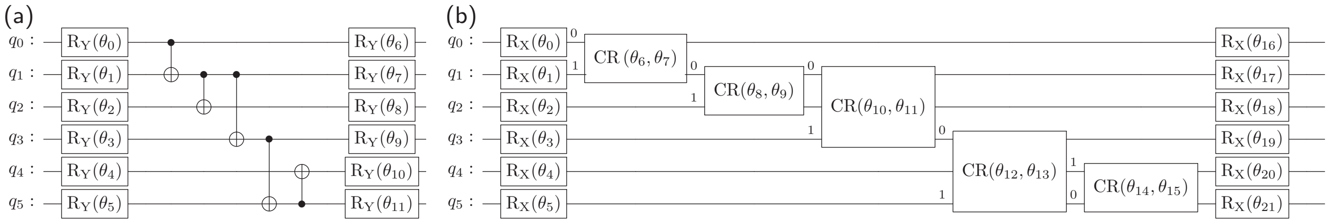

FIG. 6. H_3 *Ansätze*. (a) CNOT-based *Ansatz* in which a layer of parameterized R_Y gates is applied before and after the CNOT gates. In total, the variational form has 12 parameters. This circuit is transpiled to the $\{\sqrt{X}, R_Z,$ CNOT$\}$ basis. (b) Pulse-based *Ansatz* with 22 parameters. Each gate corresponds to a single pulse. The first and second parameters in the cross-resonance gates control the duration and amplitude, respectively, of the GaussianSquare pulse.

gates, implement echoes [46], and fix the CNOT direction; see Appendix E. Crucially, the duration of the schedule of the optimized pulses is less than one-third of the duration of the CNOT-based schedule; see Fig. 7(c). After the optimization, the optimal CR pulses have an almost maximum amplitude of 1.0 and are shorter than the pulses implementing CNOT gates; compare the pulses on the control channels in Figs. 8(a) and 8(b). This is consistent with mitigating decoherence. While, in general, short and intense pulses may induce leakage, it is not necessarily harmful. Leakage can help convergence, as observed in both simulations of pulse-based VQE [49] and gate design with optimal control [66]. Our results provide further evidence of the positive impact of short and intense pulses.

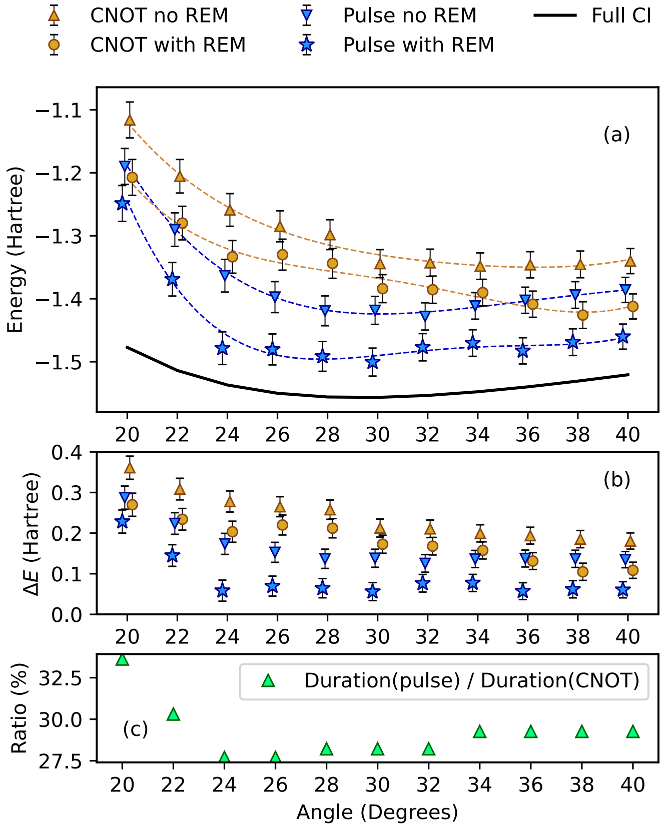

FIG. 7. Energy in H_3. (a) Sum of the electronic energy, obtained with VQE, and the repulsion energy of H_3 without readout-error mitigation (REM) (triangles) and with REM (circles and stars). The CNOT-based and pulse-based *Ansätze* of Fig. 6 are labeled CNOT and Pulse, respectively. The dashed lines are fourth-order fits. The solid black line is the full CI solution. (b) Absolute difference with respect to the ideal energy. (c) Schedule duration of the pulse-based variational form, without REM and excluding measurement pulses, expressed as a fraction of the CNOT-based variational form which lasts 9184 dt, i.e., 2.04 μs. The error bars show an upper bound on the sampling error of the estimator; see Appendix C. They are increased by a factor of two and markers are slightly x-shifted for visibility purposes.

C. Four hydrogen atoms

We now evaluate the energy of the H_4 molecule as described in Sec. III at an angle of $\alpha = 40^\circ$ only. As for H_3, we use a REALAMPLITUDE *Ansatz* for the CNOT-based VQE. The pulse-based *Ansatz* has the same two-qubit gate structure; see Fig. 9. We compare a depth-one and a depth-two CNOT-based *Ansatz*, and a depth-one pulse-based *Ansatz*, which have 16, 24, and 40 parameters, respectively. For the pulse-based *Ansatz*, we first optimize the amplitudes and durations while keeping the phases θ_8 to θ_{15} at zero. The optimization is done on *ibmq_mumbai* with COBYLA and 4096 shots per circuit. The depth-two CNOT-based and depth-one pulse-based *Ansätze* show a similar convergence profile; see Fig. 10. The pulse-based *Ansatz* achieves a minimum energy of −4.39 Hartree and the depth-two CNOT *Ansatz* achieves −4.26 Hartree.

So far, we did not optimize the phases of the cross-resonance drives in the pulse-based *Ansatz*. We therefore optimize the phase shifts while keeping the pulse durations and amplitudes fixed at the measured optimal values. The initial value of the phases shifts, $\theta_8, \dots, \theta_{15}$, is chosen at random. These phases impact the measured energy, as seen by the decrease of the green curve in Fig. 10. With the optimized phases, we measure an energy of −4.44 Hartree, i.e., a 1% improvement over the pulse-based *Ansatz* without phases.

As for H_3, the optimization favors short and intense pulse schedules; see Fig. 11. Many of the pulses have near maximum amplitude, i.e., 1, and a short duration. This is confirmed by inspecting the values of the pulse parameters during the optimization. COBYLA quickly pushes up the amplitude of the cross-resonance pulses that it requires and keeps the duration small; see Fig. 12. The best pulse-based schedule is only 20.6% of the duration of the best depth-two CNOT-based schedule; see Fig. 11.

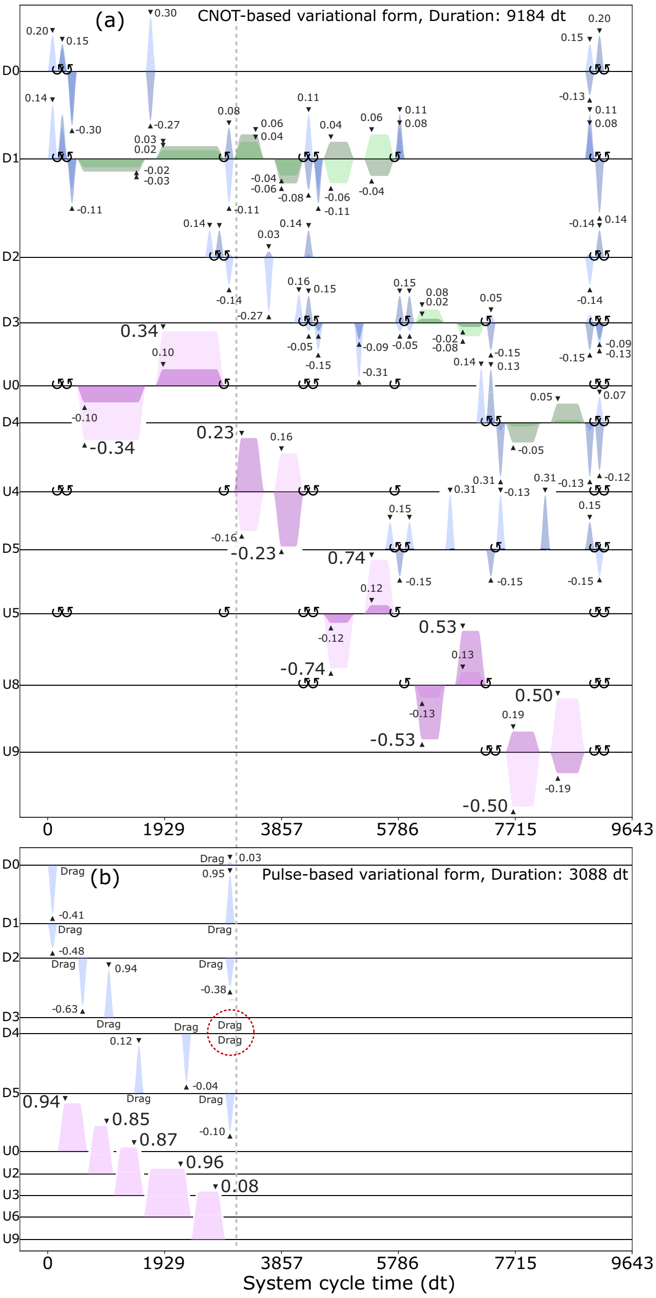

FIG. 8. Optimized pulse schedules for H_3 at $\alpha = 20^\circ$. (a) and (b) correspond to the CNOT-based and pulse-based schedules, respectively. The cross-resonance pulses in (b) are not necessarily applied on the same control channels as the CNOT gates in (a). In such a case, the role of the control and target qubits is reversed. The numbers indicate the amplitude of the pulse. The light and dark shades indicate the real and imaginary part of the pulse envelope, respectively. The green pulses in (a) correspond to rotary pulses. The dotted red circle in (b) indicates pulses in the variational form whose amplitude was set to zero by the optimizer. The control channel indexing is discussed in Appendix E. The numbers above each pulse indicate the amplitude of the pulse as a fraction of the maximum output voltage of the arbitrary waveform generator.

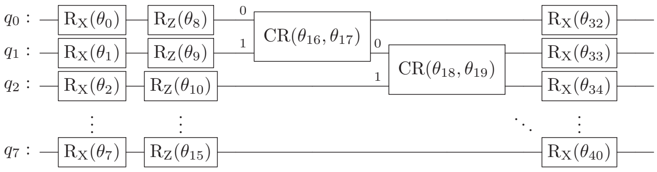

FIG. 9. H_4 pulse-based *Ansatz*. The *Ansatz* has a total of 40 parameters. We first optimize the pulse amplitudes and durations, i.e., 32 parameters, and then the remaining 8 phases in the $R_Z(\theta_i)$ gates.

V. ERROR MITIGATION

We did not use error mitigation to focus on the gains afforded by optimizing pulse parameters. Error mitigation may improve these results. For example, scalable readout-error mitigation, such as M3 [67], is easily applied to pulse-based VQE. Crucially, other known error-mitigation methods must be adapted to work with pulse-based VQE. We now discuss the challenges of performing dynamical decoupling [68], Pauli twirling [69], probabilistic error cancellation [70], and zero-noise extrapolation [71] in a pulse-based VQE.

Dynamical decoupling [72–74] suppresses non-Markovian errors by adding pulses in the idle regions of a schedule. The

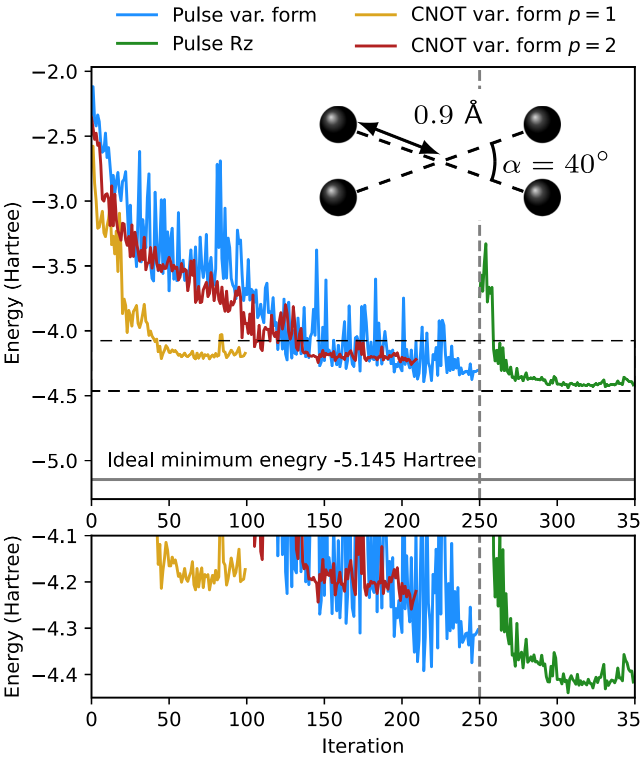

FIG. 10. Electronic energy of H_4. The gray horizontal line shows the minimum energy. The depth of the *Ansatz* is p. The bottom panel corresponds to the region between the dashed horizontal lines. The vertical gray line shows the point where we freeze the amplitudes and duration, and optimize the phase.

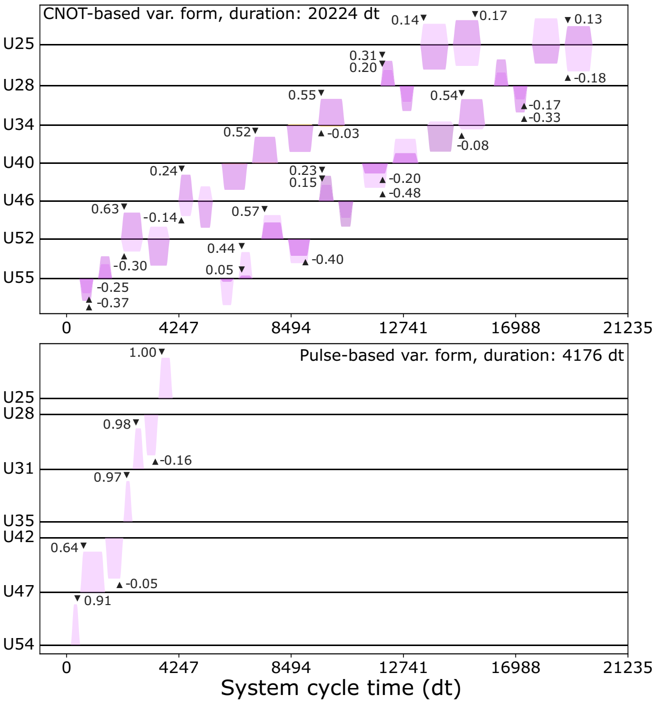

FIG. 11. Optimized pulse schedules for H$_4$. The top and bottom panels show the schedules of the depth-two CNOT- and pulse-based *Ansatz*, respectively. For visualization purposes, we only show the cross-resonance drives and omit the single-qubit pulses as well as the rotary tones in the CNOT gates.

inserted pulses mitigate the effects of decoherence [68,75] and cancel crosstalk [76,77] on transmon-based devices similar to those used here. Dynamical decoupling pulses can be added in pulse-based VQE [78] in the idle regions of the *Ansatz*. This may be less beneficial in pulse-based VQE than circuit VQE for three reasons. First, the pulse-based VQE schedules are compact and have short idle regions, as exemplified by Fig. 8. Second, idle regions change every iteration as pulse durations are optimized. Third, the errors that dynamical decoupling suppress, e.g., crosstalk and leakage, are not always detrimental in pulse-based VQE since they can help convergence. Nonetheless, for larger problems with longer idle delays, suppression of errors through a robust dynamical decoupling sequence could provide a noticeable performance improvement.

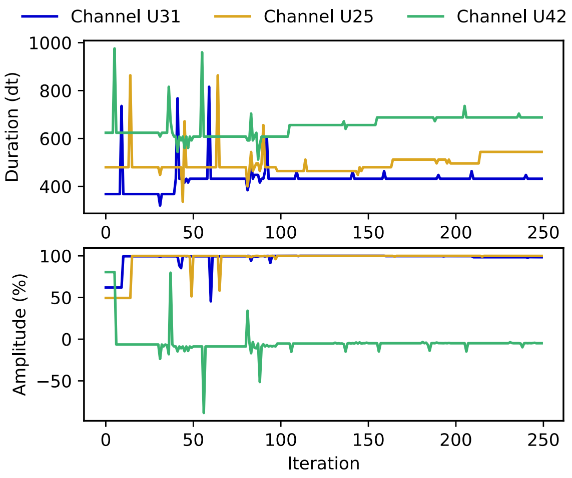

FIG. 12. Parameter optimization. The pulse parameters of the cross-resonance pulses played on the channels U25, U31, and U42, shown in Fig. 11, during the COBYLA optimization of H$_4$. The minimum duration of the GaussianSquare pulses is 256 samples due to the Gaussian flanks.

Pauli twirling [69] inserts Paulis in between noisy gates, such as CNOTs and $R_{ZZ}(\theta)$ gates [79,80], and commutes an inverse of each Pauli through the noisy gates. This scheme requires the user to know the ideal operation of the noisy gate and may therefore be harder to implement in a pulse-based VQE. For example, knowledge of the ideal cross-resonance gate could be obtained with a fit of a model to Hamiltonian tomography data. Similarly, in probabilistic error cancellation, the noise model of layers of Pauli-twirled CNOT gates is learned and corrected for in a quantum circuit by randomly inserting Pauli gates to cancel the noise on average [70]. This is harder to implement in pulse-based VQE since the noise changes throughout the optimization as the pulse parameters are varied.

In zero-noise extrapolation, an expectation value is measured several times with logically equivalent quantum circuits, but with different noise levels [71]. The noiseless expectation value is, in principle, recovered by extrapolating the noisy results to the zero-noise limit. The additional noise is introduced by stretching the pulses that implement the single- and two-qubit gates [81] or by gate folding [82–84]. Pulse stretching is hard to implement, even in gate-based approaches, since it requires intensive calibration and changes in pulse amplitude may induce nonlinear changes in the noise. Pulse stretching could be implemented with a large overhead in pulse-based VQE by performing tomography of the individual pulses and trying to reproduce the unitary part of the time evolution with a stretched pulse with weaker amplitude and longer duration. By contrast, gate folding may be easier to implement, either by inserting delay instructions or by folding a pulse P according to $P \to [R_Z(-\pi)PR_Z(\pi)P]^n$, with $n \in \mathbb{N}$ for systems in which a negative amplitude pulse is the inverse of a positive amplitude pulse under ideal circumstances.

VI. DISCUSSION AND CONCLUSION

We demonstrate on hardware that VQE delivers better results when the pulse parameters such as duration and amplitude are simultaneously optimized compared to CNOT-based *Ansätze*. For instance, a pulse-based *Ansatz* finds that the angle α that minimizes the energy of the H$_3$ system is only 2.7% away from the full CI computation, while a CNOT-based *Ansatz* measures a deviation of 24.2%. Crucially, we observed that the pulse optimization favors short and intense pulses to mitigate the effects of decoherence and energy relaxation.

Our experiments are carried out on cross-resonance-based hardware. Pulse-based VQE is also applicable to other architectures such as tunable couplers [85]. Crucially, tunable couplers support a versatile range of interactions such iSWAP, and controlled-phase generators [86] which conserve particle number. Such exchangelike gates help reduce the circuit depth of variational *Ansätze* [11,87]. We therefore expect that such an architecture may provide even better pulse-based *Ansätze*. Pulse-based VQE is also applicable to other quantum computing architectures capable of pulse-shaping and variational algorithms. For example, trapped ions and Rydberg atoms are both amenable to optimal control [88,89] and VQE [90,91]. We anticipate that such systems will also benefit from the shorter schedules of pulse-based VQE as long as they are fast enough.

Running variational algorithms on hardware is time consuming. This makes speed a key resource for quantum computers [92]. At the time of writing, *ibmq_mumbai* reported 1800 circuit layer operations per second (CLOPS). Increasing the CLOPS is key to make variational algorithms scalable. Short-duration pulse-based *Ansätze* may also help increase the CLOPS once run-time compilation and data transfer bottlenecks are removed. Such reductions of quantum processing time are similar to restless measurements which forego qubit reset in calibration [26] and optimal control schemes [27,93]. Methods that reduce the number of shots, such as positive operator valued measures [94,95], are compatible with pulse-based VQE and may further reduce execution times.

The pulse-based variational forms shown here have shorter schedules, but contain more parameters to optimize than gate-based ones. This may make them more expressive, but increases their optimization cost. Future work on pulse-based VQE will need to scale up these variational forms, while keeping their parameter numbers reasonable and retaining an adequate expressiveness. We leave it to future work to investigate the expressiveness and number of parameters in pulse-based VQE in a study akin to existing research for circuit-based *Ansätze* [96]. Methods such as adaptive derivative-assembled pseudo-trotter ansatz variational quantum eigensolver (ADAPT-VQE) which grow the variational form one operator at a time may be modified and applied to pulse-based VQEs [19,97]. Algorithms such as wavefunction adapted Hamiltonian through orbital rotation (WAHTOR) that exploit symmetries in the Hamiltonian by molecular orbital rotations could also be adapted to pulse-based *Ansätze* [60]. Furthermore, adapting state-of-the-art error-mitigation methods to pulse-based VQE requires more research, as discussed in Sec. V.

In summary, we showed a pulse-based *Ansatz* inspired by hardware constraints. Our results demonstrated that pulse-based variational forms are a viable way to reduce schedule duration in hardware-native *Ansätze* to fight decoherence and increase the accuracy of VQE. The quality of our results is still beyond chemical accuracy. As for conventional CR-based approaches, accurate results are only possible through the implementation of error-mitigation schemes. The combination of pulse-based VQE and error mitigation will be the subject of future studies. These may also include the investigation of pulse-shaping methods that are closer to chemistry-inspired *Ansätze* such as the unitary coupled cluster approach [98].

ACKNOWLEDGMENTS

This research was supported by the NCCR MARVEL, a National Centre of Competence in Research, funded by the Swiss National Science Foundation (Grant No. 205602). This research has received funding from the European Union's Horizon 2020 research and innovation program under the Marie Skłodowska-Curie Grant Agreement No. 955479. IBM, the IBM logo, and ibm.com are trademarks of International Business Machines Corp., registered in many jurisdictions worldwide. Other product and service names might be trademarks of IBM or other companies. The current list of IBM trademarks is available (see [99]).

APPENDIX A: NUMERICAL SIMULATIONS OF CROSS-RESONANCE PULSE-BASED VQE

We simulate pulse-based VQE with both QISKIT AER and QISKIT DYNAMICS. The pulse-based *Ansatz*, e.g., Fig. 6(b), has custom CR instructions, each encapsulating a GaussianSquare pulse as a schedule. Before simulating the quantum circuit in QISKIT AER, we run a transpiler pass that identifies any CR instructions with a pulse schedule. When such an instruction is found, we attach to it a unitary matrix obtained from a QISKIT DYNAMICS simulation. This simulation solves the time evolution of a two-qubit system only, with a Hamiltonian given by Eq. (1). The coefficients of $\bar{H}_{cr}$ are measured on the hardware with QISKIT EXPERIMENTS [57].

We now consider the hydrogen molecule starting from the 0.74 Å bond distance. We run a noiseless VQE for each point on the curve with COBYLA and the QASM SIMULATOR in QISKIT with 8192 shots. The variational parameters $\boldsymbol{\theta}$ in each optimization are initialized with the optimal parameters of the nearest considered bond distance, with the exception of $d = 0.74$ Å for which random parameters were chosen. We compare a REALAMPLITUDE depth-one CNOT-based variational wave function to two pulse-based variational forms, with and without R_Z rotations before the cross-resonance gates. Moreover, each pulse-based variational form is studied at depths one and two; see Fig. 13.

The energy obtained from the depth-one pulse-based *Ansatz* shows that a single cross-resonance pulse is not sufficiently expressive; see blue markers in Fig. 13. Indeed, a depth-two pulse-based *Ansatz*, i.e., two cross-resonance tones, is required to get energies close to the full CI dissociation curve; see red circles in Fig 13. Furthermore, adding R_Z gates to control the phase of the cross-resonance tones allows us to recover almost all of the system's correlation energy; see the red stars. The CNOT-based *Ansatz* directly engineers the ground state of H_2.

APPENDIX B: PULSE PARAMETER WRAPPING

QISKIT PULSE allows users to manipulate quantum computers at the level of pulses by specifying schedules of pulses [42,43]. The pulses must satisfy hardware-imposed requirements. First, the complex-valued pulse amplitude is expressed as a fraction of the maximum output voltage of the arbitrary waveform generator (AWG) and must therefore be restricted to the interval $[-1, 1]$. Second, the duration of a pulse, expressed in the number of AWG samples, must be a multiple of 16 to be loaded in the AWG memory. Third, the duration must be kept large enough to prevent the width of the flat top from being negative; see Fig. 14(a). To impose these constraints, we introduce the concept of a parameter wrapper. In a pulse-based variational form, the optimizer optimizes the parameters θ_i. However, the parameters used to construct the pulses are the output of functions that wrap θ_i, i.e., $f_i(\theta_i)$. The amplitude

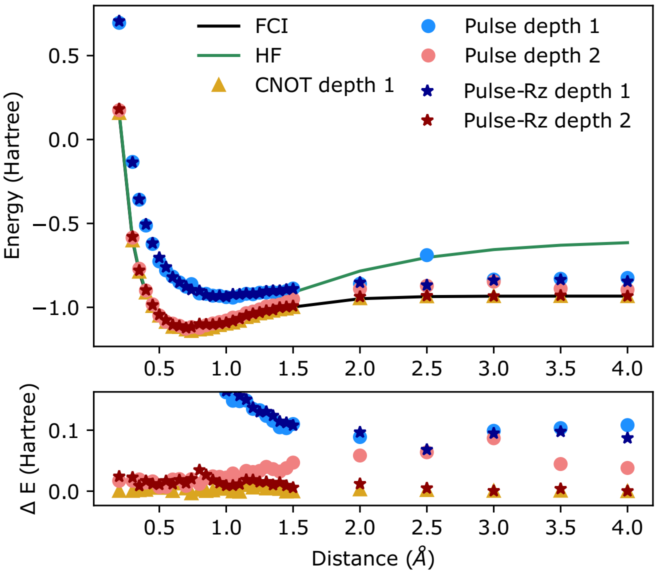

FIG. 13. Simulated H_2 dissociation curves. The total energy is plotted against the distance between the two H atoms. The yellow triangles correspond to the CNOT-based *Ansatz*. The circles and stars correspond to the pulse-based wave function without and with the R_Z rotations, respectively. The black and green lines represent the full CI and Hartree-Fock energies, respectively. The bottom panel shows the absolute energy difference between the VQE simulations and the full CI energy.

is restricted to the interval $[-1, 1]$ by a sinusoidal function; see Fig. 14(c). The duration is restricted to the interval [256, 1040] samples by a sinusoidal function whose codomain is restricted to multiples of 16. The lower bound ensures that the width does not become negative, and the upper bound, loosely chosen based on the strength of ω_{ZX}, prevents the pulse from becoming too long.

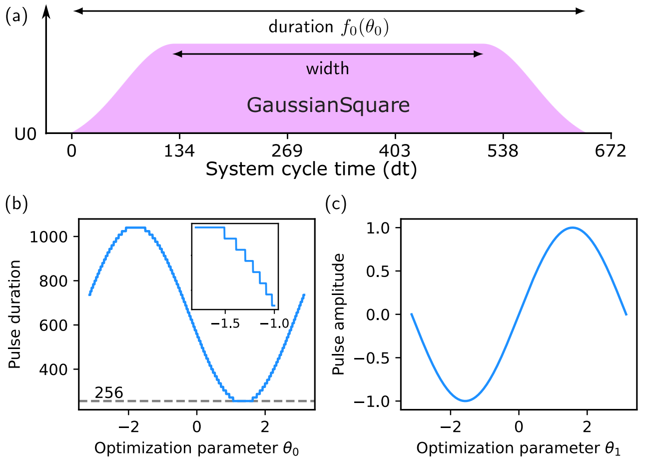

FIG. 14. Example of wrapper functions. (a) GaussianSquare pulse with duration $f_0(\theta_0)$ and amplitude $f_1(\theta_1)$. (b) Duration wrapper that relates the optimization parameter θ_0 to the pulse duration through a sinusoidal function vertically discretized to multiples of 16. The minimum duration is set to 256 samples, which corresponds to a width of 0. (c) Amplitude wrapper that relates the optimization parameter θ_1 to the amplitude of the pulse through a sinusoidal function.

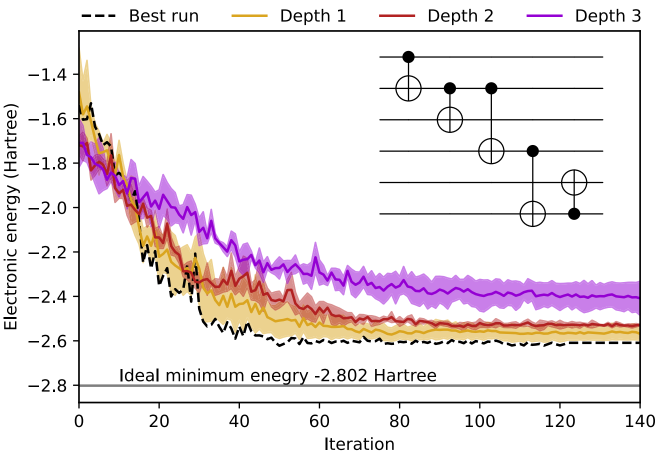

FIG. 15. VQE on H_3 with different depths. The inset shows the structure of the entangler that was repeated p times with $p + 1$ layers of parameterized $R_Y(\theta)$ gates. The bond distance is 1.43 Å and the angle is 40°. The solid lines and shaded areas show the mean and standard deviation, respectively, of three runs. The dashed black line shows the best run, which was a depth-one run.

APPENDIX C: STATISTICAL ERROR BOUND

Here we derive an upper bound for the worst-case statistical sampling error $\epsilon_{\max}$ of the energy expectation values shown as error bars in Figs. 4 and 7. We partition the Hamiltonian H of each hydrogen system into M groups of mutually qubitwise commuting Pauli terms,

$$H = \sum_{i=1}^{M}\sum_{j=1}^{m_i} c_{ij}P_{ij}. \tag{C1}$$

Here, m_i is the number of Pauli terms in group i, P_{ij} is the jth Pauli in group i, and c_{ij} are coefficients. The number of shots used to estimate the Paulis in group i is $n_i = 4096\,\forall\, i = 1, \dots, M$. Since every group is estimated independently, the total variance ϵ^2 of the estimator of $\langle H\rangle$ is the sum of the standard errors of every group. We can thus compute the following bound:

$$\epsilon^2 = \sum_{i=1}^{M}\frac{1}{n_i}\mathrm{Var}\left[\sum_{j=1}^{m_i} c_{ij}P_{ij}\right] \tag{C2}$$

$$= \sum_{i=1}^{M}\frac{1}{n_i}\sum_{j,j'=1}^{m_i} c_{ij}c_{ij'}\mathrm{Cov}[P_{ij}, P_{ij'}] \tag{C3}$$

$$\leqslant \sum_{i=1}^{M}\frac{1}{n_i}\sum_{j,j'=1}^{m_i} |c_{ij}c_{ij'}|\sqrt{\mathrm{Var}[P_{ij}]\mathrm{Var}[P_{ij'}]} \tag{C4}$$

$$\leqslant \sum_{i=1}^{M}\frac{1}{n_i}\sum_{j,j'=1}^{m_i} |c_{ij}c_{ij'}|. \tag{C5}$$

We used the Cauchy-Schwarz inequality and the fact that $\mathrm{Var}[P_{i,j}] \leqslant 1$. The standard error of the estimator for any state

TABLE I. Strength of the terms in the effective cross-resonance model for *ibm_mumbai* and *ibmq_mumbai*. All numbers are in kHz and were measured with a single Gaussian square pulse with unit amplitude.

ibm_lagos							*ibmq_mumbai*						
Qubits	ω_{ZX}	ω_{ZY}	ω_{ZZ}	ω_{IX}	ω_{IY}	ω_{IZ}	Qubits	ω_{ZX}	ω_{ZY}	ω_{ZZ}	ω_{IX}	ω_{IY}	ω_{IZ}
(0, 1)	872(2)	705(2)	−6(2)	−839(2)	−584(2)	14(2)	(12, 13)	−930(1)	−637(2)	93(1)	−214(1)	−143(2)	6(1)
(1, 2)	−1803(2)	−1056(4)	7(3)	−490(2)	−244(4)	−49(3)	(13, 14)	1481(1)	294(4)	23(2)	−765(1)	−170(4)	−74(2)
(1, 3)	−2430(3)	858(10)	−88(8)	4168(3)	−1459(10)	−124(8)	(14, 16)	520(1)	−450(2)	−53(2)	−589(1)	533(2)	−140(2)
(3, 5)	194(1)	641(1)	−48(1)	47(1)	70(1)	39(1)	(16, 19)	768(1)	−295(2)	53(1)	−341(1)	131(2)	−19(1)
(5, 4)	−383(4)	1660(1)	−99(2)	−89(4)	364(1)	83(2)	(19, 22)	−1078(1)	734(2)	137(2)	−83(1)	68(2)	−64(2)
							(22, 25)	−1110(1)	−509(2)	4(2)	396(1)	181(2)	−40(2)
							(25, 26)	631(2)	467(3)	1(2)	1228(2)	917(3)	−20(2)

is thus upper bounded by

$$\epsilon_{\max} = \sqrt{\sum_{i=1}^{M} \frac{1}{n_i} \sum_{j,j'=1}^{m_i} |c_{i,j} c_{i,j'}|}. \qquad \text{(C6)}$$

APPENDIX D: ADDITIONAL DATA FOR THE THREE HYDROGEN ATOMS

Here, we present additional data on the H_3 system. We investigate the effect of the depth of the CNOT-based variational form on the measured energy. The data, made of nine hardware runs, with three at each depth $p \in \{1, 2, 3\}$, are acquired on *ibm_lagos*. Each run has a different initial point chosen uniformly in the interval $[0, \pi]^{6(p+1)}$. Under these settings, we observe that the best results are obtained with a depth-one *Ansatz*; see Fig. 15. *Ansätze* with depth $p > 1$ did not result in a lower energy than $p = 1$. This may be due to the COBYLA optimizer getting stuck in local minima or due to the added noise of the deeper circuits. Error-mitigation methods may help to overcome the added noise, while methods that progressively build up the *Ansatz* may help tackle local minima [97]. The jobs took a total of 71 ± 9, 102 ± 2, and 99 ± 0 minutes of classical and quantum compute time, for depths one, two, and three, respectively, as reported by *ibm_lagos*. Each circuit was executed with 4096 shots.

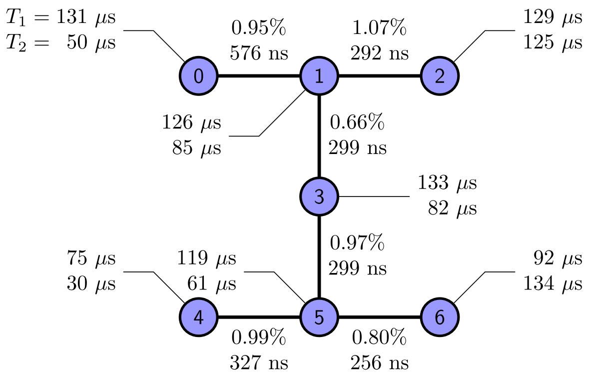

FIG. 16. Coupling map of *ibm_lagos*. The numbers attached to each qubit represent the T_1 and T_2 times as reported by the backend. The top and bottom numbers of each edge indicate the error of the CNOT gate and its duration, respectively.

APPENDIX E: HARDWARE

We now describe the hardware on which the data were gathered. The H_2 molecule and the H_3 system were both run on the seven-qubit IBM Quantum device *ibm_lagos*, whose coupling map is shown in Fig. 16 and Table I. Here, the CNOT gates are implemented with echoed cross-resonance pulses. Since calibration is time consuming, the backends only calibrate one CNOT gate for each pair of coupled qubits (i, j). This CNOT gate is referred to as *hardware native*. The CNOT gate in the reverse direction (j, i) is implemented with additional single-qubit pulses and the hardware-native CNOT gate. The CNOT-based and pulse-based variational forms in the main text sometimes differ in the control channels on which they apply CR pulses, despite the fact that the CNOT and CR gates are applied on the same qubit pair (i, j). This is because the desired CNOT gate may not be hardware native. For convenience, we summarize the configuration of the control channels as (i, j): Uk, where Uk is the control channel which drives qubit i, the control, at the frequency of qubit j, the target. On *ibm_lagos*, the control channel configuration is (0, 1): $U0$, (1, 0): $U1$, (1, 2): $U2$, (2, 1): $U4$, (1, 3): $U3$, (3, 1): $U5$, (3, 5): $U6$, (5, 3): $U8$, (4, 5): $U7$, and (5, 4): $U9$.

The H_4 system was run on the linearly coupled qubits 12, 13, 14, 16, 19, 22, 25, and 26 of the 27-qubit system *ibmq_mumbai*. The properties of these qubits are summarized in Fig. 17 and Table I.

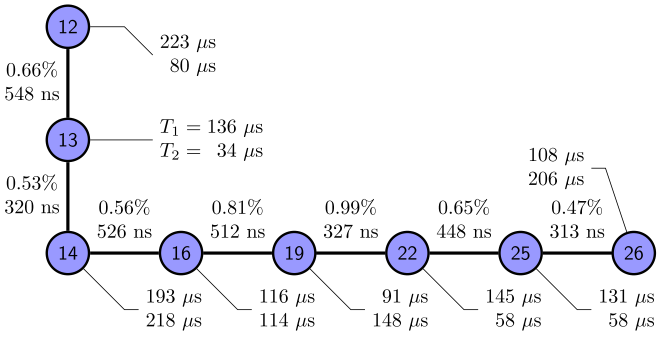

FIG. 17. Qubits of *ibmq_mumbai* to run H_4. The numbers attached to each qubit represent the T_1 and T_2 times as reported by the backend. The top and bottom numbers of each edge indicate the error of the CNOT gate and its duration, respectively.

[1] N. Moll, P. Barkoutsos, L. S. Bishop, J. M. Chow, A. Cross, D. J. Egger, S. Filipp, A. Fuhrer, J. M. Gambetta *et al.*, Quantum optimization using variational algorithms on near-term quantum devices, Quantum Sci. Technol. **3**, 030503 (2018).

[2] P. J. J. O'Malley, R. Babbush, I. D. Kivlichan, J. Romero, J. R. McClean, R. Barends, J. Kelly, P. Roushan, A. Tranter *et al.*, Scalable Quantum Simulation of Molecular Energies, Phys. Rev. X **6**, 031007 (2016).

[3] J. R. McClean, J. Romero, R. Babbush, and A. Aspuru-Guzik, The theory of variational hybrid quantum-classical algorithms, New J. Phys. **18**, 023023 (2016).

[4] P. J. Ollitrault, S. Jandura, A. Miessen, I. Burghardt, R. Martinazzo, F. Tacchino, and I. Tavernelli, Quantum algorithms for grid-based variational time evolution, arXiv:2203.02521.

[5] M. Motta and J. E. Rice, Emerging quantum computing algorithms for quantum chemistry, WIREs Comput. Mol. Sci. **12**, e1580 (2022).

[6] T. E. O'Brien, G. Anselmetti, F. Gkritsis, V. E. Elfving, S. Polla, W. J. Huggins, O. Oumarou, K. Kechedzhi, D. Abanin *et al.*, Purification-based quantum error mitigation of pair-correlated electron simulations, arXiv:2210.10799.

[7] V. Havlicek, A. D. Corcoles, K. Temme, A. W. Harrow, A. Kandala, J. M. Chow, and J. M. Gambetta, Supervised learning with quantum-enhanced feature spaces, Nature (London) **567**, 209 (2019).

[8] A. Abbas, D. Sutter, C. Zoufal, A. Lucchi, A. Figalli, and S. Woerner, The power of quantum neural networks, Nat. Comput. Sci. **1**, 403 (2021).

[9] A. Melo, N. Earnest-Noble, and F. Tacchino, Pulse-efficient quantum machine learning, arXiv:2211.01383.

[10] E. Farhi, J. Goldstone, and S. Gutmann, A quantum approximate optimization algorithm, arXiv:1411.4028.

[11] P. Kl. Barkoutsos, J. F. Gonthier, I. Sokolov, N. Moll, G. Salis, A. Fuhrer, M. Ganzhorn, D. J. Egger, M. Troyer *et al.*, Quantum algorithms for electronic structure calculations: Particle-hole Hamiltonian and optimized wave-function expansions, Phys. Rev. A **98**, 022322 (2018).

[12] M. P. Harrigan, K. J. Sung, M. Neeley, K. J. Satzinger, F. Arute, K. Arya, J. Atalaya, J. C. Bardin, R. Barends, S. Boixo *et al.*, Quantum approximate optimization of nonplanar graph problems on a planar superconducting processor, Nat. Phys. **17**, 332 (2021).

[13] G. C. Santra, F. Jendrzejewski, P. Hauke, and D. J. Egger, Squeezing and quantum approximate optimization, arXiv:2205.10383.

[14] E. Pelofske, A. Bärtschi, and S. Eidenbenz, Quantum annealing vs. QAOA: 127 qubit higher-order Ising problems on NISQ computers, in *High Performance Computing*, edited by A. Bhatele, J. Hammond, M. Baboulin, and C. Kruse (Springer Nature, Cham, 2023), pp. 240–258.

[15] S. H. Sack and D. J. Egger, Large-scale quantum approximate optimization on non-planar graphs with machine learning noise mitigation, arXiv:2307.14427.

[16] J. Weidenfeller, L. C. Valor, J. Gacon, C. Tornow, L. Bello, S. Woerner, and D. J. Egger, Scaling of the quantum approximate optimization algorithm on superconducting qubit based hardware, Quantum **6**, 870 (2022).

[17] A. Kandala, A. Mezzacapo, K. Temme, M. Takita, M. Brink, J. M. Chow, and J. M. Gambetta, Hardware-efficient variational quantum eigensolver for small molecules and quantum magnets, Nature (London) **549**, 242 (2017).

[18] I. G. Ryabinkin, T.-C. Yen, S. N. Genin, and A. F. Izmaylov, Qubit coupled cluster method: A systematic approach to quantum chemistry on a quantum computer, J. Chem. Theor. Comput. **14**, 6317 (2018).

[19] H. R. Grimsley, S. E. Economou, E. Barnes, and N. J. Mayhall, An adaptive variational algorithm for exact molecular simulations on a quantum computer, Nat. Commun. **10**, 3007 (2019).

[20] J. Lee, W. J. Huggins, M. Head-Gordon, and K. B. Whaley, Generalized unitary coupled cluster wave functions for quantum computation, J. Chem. Theory Comput. **15**, 311 (2019).

[21] D. J. Egger, J. Mareček, and S. Woerner, Warm-starting quantum optimization, Quantum **5**, 479 (2021).

[22] P. Krantz, M. Kjaergaard, F. Yan, T. P. Orlando, S. Gustavsson, and W. D. Oliver, A quantum engineer's guide to superconducting qubits, Appl. Phys. Rev. **6**, 021318 (2019).

[23] M. Kjaergaard, M. E. Schwartz, J. Braumüller, P. Krantz, J. I.-J. Wang, S. Gustavsson, and W. D. Oliver, Superconducting qubits: Current state of play, Annu. Rev. Condens. Matter Phys. **11**, 369 (2020).

[24] J. Koch, T. M. Yu, J. M. Gambetta, A. A. Houck, D. I. Schuster, J. Majer, A. Blais, M. H. Devoret, S. M. Girvin, and R. J. Schoelkopf, Charge-insensitive qubit design derived from the cooper pair box, Phys. Rev. A **76**, 042319 (2007).

[25] D. C. McKay, C. J. Wood, S. Sheldon, J. M. Chow, and J. M. Gambetta, Efficient Z gates for quantum computing, Phys. Rev. A **96**, 022330 (2017).

[26] C. Tornow, N. Kanazawa, W. E. Shanks, and D. J. Egger, Minimum Quantum Run-Time Characterization and Calibration Via Restless Measurements with Dynamic Repetition Rates, Phys. Rev. Appl. **17**, 064061 (2022).

[27] M. Werninghaus, D. J. Egger, F. Roy, S. Machnes, F. K. Wilhelm, and S. Filipp, Leakage reduction in fast superconducting qubit gates via optimal control, npj Quantum Inf. **7**, 14 (2021).

[28] S. J. Glaser, U. Boscain, T. Calarco, C. P. Koch, W. Köckenberger, R. Kosloff, I. Kuprov, B. Luy, S. Schirmer *et al.*, Training Schrödinger's cat: Quantum optimal control, Eur. Phys. J. D **69**, 279 (2015).

[29] U. Boscain, M. Sigalotti, and D. Sugny, Introduction to the Pontryagin maximum principle for quantum optimal control, PRX Quantum **2**, 030203 (2021).

[30] C. P. Koch, U. Boscain, T. Calarco, G. Dirr, S. Filipp, S. J. Glaser, R. Kosloff, S. Montangero, T. Schulte-Herbrüggen *et al.*, Quantum optimal control in quantum technologies. strategic report on current status, visions and goals for research in europe, EPJ Quantum Technol. **9**, 19 (2022).

[31] S. Bao, S. Kleer, R. Wang, and A. Rahmani, Optimal control of superconducting gmon qubits using Pontryagin's minimum principle: Preparing a maximally entangled state with singular bang-bang protocols, Phys. Rev. A **97**, 062343 (2018).

[32] M. Mališ, P. Kl. Barkoutsos, M. Ganzhorn, S. Filipp, D. J. Egger, S. Bonella, and I. Tavernelli, Local control theory for superconducting qubits, Phys. Rev. A **99**, 052316 (2019).

[33] D. J. Egger and F. K. Wilhelm, Optimized controlled-Z gates for two superconducting qubits coupled through a resonator, Supercond. Sci. Technol. **27**, 014001 (2013).

[34] J. Kelly, R. Barends, B. Campbell, Y. Chen, Z. Chen, B. Chiaro, A. Dunsworth, A. G. Fowler, I. C. Hoi *et al.*, Optimal Quantum

Control Using Randomized Benchmarking, Phys. Rev. Lett. **112**, 240504 (2014).
[35] A. Winick, J. J. Wallman, and J. Emerson, Simulating and Mitigating Crosstalk, Phys. Rev. Lett. **126**, 230502 (2021).
[36] C. P. Koch, Controlling open quantum systems: Tools, achievements, and limitations, J. Phys.: Condens. Matter **28**, 213001 (2016).
[37] D. J. Egger and F. K. Wilhelm, Optimal control of a quantum measurement, Phys. Rev. A **90**, 052331 (2014).
[38] S. Boutin, C. K. Andersen, J. Venkatraman, A. J. Ferris, and A. Blais, Resonator reset in circuit QED by optimal control for large open quantum systems, Phys. Rev. A **96**, 042315 (2017).
[39] D. J. Egger and F. K. Wilhelm, Adaptive Hybrid Optimal Quantum Control for Imprecisely Characterized Systems, Phys. Rev. Lett. **112**, 240503 (2014).
[40] N. Wittler, F. Roy, K. Pack, M. Werninghaus, A. S. Roy, D. J. Egger, S. Filipp, F. K. Wilhelm, and S. Machnes, Integrated Tool Set for Control, Calibration, and Characterization of Quantum Devices Applied to Superconducting Qubits, Phys. Rev. Appl. **15**, 034080 (2021).
[41] A. B. Magann, C. Arenz, M. D. Grace, T.-S. Ho, R. L. Kosut, J. R. McClean, H. A. Rabitz, and M. Sarovar, From pulses to circuits and back again: A quantum optimal control perspective on variational quantum algorithms, PRX Quantum **2**, 010101 (2021).
[42] D. C. McKay, T. Alexander, L. Bello, M. J. Biercuk, L. Bishop, J. Chen, J. M. Chow, A. D. Córcoles, D. J. Egger *et al.*, Qiskit backend specifications for openQASM and openpulse experiments, arXiv:1809.03452.
[43] T. Alexander, N. Kanazawa, D. J. Egger, L. Capelluto, C. J. Wood, A. Javadi-Abhari, and D. C. McKay, Qiskit pulse: Programming quantum computers through the cloud with pulses, Quantum Sci. Technol. **5**, 044006 (2020).
[44] A. Peruzzo, J. McClean, P. Shadbolt, M.-H. Yung, X.-Q. Zhou, P. J. Love, A. Aspuru-Guzik, and J. L. O'Brien, A variational eigenvalue solver on a photonic quantum processor, Nat. Commun. **5**, 4213 (2014).
[45] Z. Liang, H. Wang, J. Cheng, Y. Ding, H. Ren, Z. Gao, Z. Hu, D. S. Boning, X. Qian, S. Han *et al.*, Variational quantum pulse learning, in *Proceedings of the 2022 IEEE International Conference on Quantum Computing and Engineering (QCE)* (IEEE Computer Society, Los Alamitos, CA, 2022), pp. 556–565.
[46] S. Sheldon, E. Magesan, J. M. Chow, and J. M. Gambetta, Procedure for systematically tuning up cross-talk in the cross-resonance gate, Phys. Rev. A **93**, 060302(R) (2016).
[47] Z. Liang, J. Cheng, H. Ren, H. Wang, F. Hua, Y. Ding, F. Chong, S. Han, Y. Shi, and X. Qian, NAPA: Intermediate-level Variational Native-pulse Ansatz for Variational Quantum Algorithms, arXiv:2208.01215.
[48] O. R. Meitei, B. T. Gard, G. S. Barron, D. P. Pappas, S. E. Economou, E. Barnes, and N. J. Mayhall, Gate-free state preparation for fast variational quantum eigensolver simulations, npj Quantum Inf. **7**, 155 (2021).
[49] A. Asthana, C. Liu, O. R. Meitei, S. E. Economou, E. Barnes, and N. J. Mayhall, Minimizing state preparation times in pulse-level variational molecular simulations, arXiv:2203.06818.
[50] D. Meirom and S. H. Frankel, PANSATZ: Pulse-based ansatz for variational quantum algorithms, arXiv:2212.12911.
[51] C. Rigetti and M. Devoret, Fully microwave-tunable universal gates in superconducting qubits with linear couplings and fixed transition frequencies, Phys. Rev. B **81**, 134507 (2010).
[52] L. E. Fischer, A. Chiesa, F. Tacchino, D. J. Egger, S. Carretta, and I. Tavernelli, Universal Qudit Gate Synthesis for Transmons, PRX Quantum **4**, 030327 (2023).
[53] E. Magesan and J. M. Gambetta, Effective Hamiltonian models of the cross-resonance gate, Phys. Rev. A **101**, 052308 (2020).
[54] N. Sundaresan, I. Lauer, E. Pritchett, E. Magesan, P. Jurcevic, and J. M. Gambetta, Reducing unitary and spectator errors in cross resonance with optimized rotary echoes, PRX Quantum **1**, 020318 (2020).
[55] M. Ibrahim, H. Mohammadbagherpoor, C. Rios, N. T. Bronn, and G. T. Byrd, Evaluation of parameterized quantum circuits with cross-resonance pulse-driven entanglers, IEEE Trans. Quantum Eng. **3**, 1 (2022).
[56] N. Earnest, C. Tornow, and D. J. Egger, Pulse-efficient circuit transpilation for quantum applications on cross-resonance-based hardware, Phys. Rev. Res. **3**, 043088 (2021).
[57] N. Kanazawa, D. J. Egger, Y. Ben-Haim, H. Zhang, W. E. Shanks, G. Aleksandrowicz, and C. J. Wood, Qiskit experiments: A PYTHON package to characterize and calibrate quantum computers, J. Open Source Softw. **8**, 5329 (2023).
[58] G. Greene-Diniz and D. Muñoz Ramo, Generalized unitary coupled cluster excitations for multireference molecular states optimized by the variational quantum eigensolver, Intl. J. Quantum Chem. **121**, e26352 (2021).
[59] J. T. Seeley, M. J. Richard, and P. J. Love, The Bravyi-Kitaev transformation for quantum computation of electronic structure, J. Chem. Phys. **137**, 224109 (2012).
[60] L. Ratini, C. Capecci, F. Benfenati, and L. Guidoni, Wave function adapted Hamiltonians for quantum computing, J. Chem. Theory Comput. **18**, 899 (2022).
[61] M. Rossmannek, P. Kl. Barkoutsos, P. J. Ollitrault, and I. Tavernelli, Quantum HF/DFT-embedding algorithms for electronic structure calculations: Scaling up to complex molecular systems, J. Chem. Phys. **154**, 114105 (2021).
[62] M. Rossmannek, F. Pavošević, A. Rubio, and I. Tavernelli, Quantum embedding method for the simulation of strongly correlated systems on quantum computers, J. Phys. Chem. Lett. **14**, 3491 (2023).
[63] Qiskit contributors, Qiskit: An open-source framework for quantum computing (2023), doi:10.5281/zenodo.2573505.
[64] S. Machnes, E. Assémat, D. Tannor, and F. K. Wilhelm, Tunable, Flexible, and Efficient Optimization of Control Pulses for Practical Qubits, Phys. Rev. Lett. **120**, 150401 (2018).
[65] F. Motzoi, J. M. Gambetta, P. Rebentrost, and F. K. Wilhelm, Simple Pulses for Elimination of Leakage in Weakly Nonlinear Qubits, Phys. Rev. Lett. **103**, 110501 (2009).
[66] R. Schutjens, F. A. Dagga, D. J. Egger, and F. K. Wilhelm, Single-qubit gates in frequency-crowded transmon systems, Phys. Rev. A **88**, 052330 (2013).
[67] P. D. Nation, H. Kang, N. Sundaresan, and J. M. Gambetta, Scalable mitigation of measurement errors on quantum computers, PRX Quantum **2**, 040326 (2021).
[68] B. Pokharel, N. Anand, B. Fortman, and D. A. Lidar, Demonstration of Fidelity Improvement Using Dynamical Decoupling with Superconducting Qubits, Phys. Rev. Lett. **121**, 220502 (2018).
[69] J. J. Wallman and J. Emerson, Noise tailoring for scalable

quantum computation via randomized compiling, Phys. Rev. A **94**, 052325 (2016).

[70] E. van den Berg, Z. K. Minev, A. Kandala, and K. Temme, Probabilistic error cancellation with sparse Pauli-Lindblad models on noisy quantum processors, Nat. Phys. **19**, 1116 (2023).

[71] K. Temme, S. Bravyi, and J. M. Gambetta, Error Mitigation for Short-Depth Quantum Circuits, Phys. Rev. Lett. **119**, 180509 (2017).

[72] L. Viola and S. Lloyd, Dynamical suppression of decoherence in two-state quantum systems, Phys. Rev. A **58**, 2733 (1998).

[73] P. Zanardi, Symmetrizing evolutions, Phys. Lett. A **258**, 77 (1999).

[74] D. Vitali and P. Tombesi, Using parity kicks for decoherence control, Phys. Rev. A **59**, 4178 (1999).

[75] P. Jurcevic, A. Javadi-Abhari, L. S. Bishop, I. Lauer, D. F. Bogorin, M. Brink, L. Capelluto, O. Günlük, T. Itoko, N. Kanazawa *et al.*, Demonstration of quantum volume 64 on a superconducting quantum computing system, Quantum Sci. Technol. **6**, 025020 (2021).

[76] V. Tripathi, H. Chen, M. Khezri, K.-W. Yip, E. M. Levenson-Falk, and D. A. Lidar, Suppression of Crosstalk in Superconducting Qubits Using Dynamical Decoupling, Phys. Rev. Appl. **18**, 024068 (2022).

[77] B. Pokharel and D. Lidar, Better-than-classical grover search via quantum error detection and suppression, arXiv:2211.04543.

[78] G. S. Ravi, K. N. Smith, P. Gokhale, A. Mari, N. Earnest, A. Javadi-Abhari, and F. T. Chong, Vaqem: A variational approach to quantum error mitigation, in *Proceedings of the 2022 IEEE International Symposium on High-Performance Computer Architecture (HPCA)* (IEEE Computer Society, Washington, DC, 2022), pp. 288–303.

[79] Y. Kim, C. J. Wood, T. J. Yoder, S. T. Merkel, J. M. Gambetta, K. Temme, and A. Kandala, Scalable error mitigation for noisy quantum circuits produces competitive expectation values, Nat. Phys. **19**, 752 (2023).

[80] A. C. Vazquez, D. J. Egger, D. Ochsner, and S. Woerner, Well-conditioned multi-product formulas for hardware-friendly Hamiltonian simulation, Quantum **7**, 1067 (2023).

[81] A. Kandala, K. Temme, A. D. Córcoles, A. Mezzacapo, J. M. Chow, and J. M. Gambetta, Error mitigation extends the computational reach of a noisy quantum processor, Nature (London) **567**, 491 (2019).

[82] E. F. Dumitrescu, A. J. McCaskey, G. Hagen, G. R. Jansen, T. D. Morris, T. Papenbrock, R. C. Pooser, D. J. Dean, and P. Lougovski, Cloud Quantum Computing of an Atomic Nucleus, Phys. Rev. Lett. **120**, 210501 (2018).

[83] T. Giurgica-Tiron, Y. Hindy, R. LaRose, A. Mari, and W. J. Zeng, Digital zero noise extrapolation for quantum error mitigation, in *Proceedings of the 2020 IEEE International Conference on Quantum Computing and Engineering (QCE)* (IEEE, Piscataway, NJ, 2020).

[84] N. Stamatopoulos, D. J. Egger, Y. Sun, C. Zoufal, R. Iten, N. Shen, and S. Woerner, Option pricing using quantum computers, Quantum **4**, 291 (2020).

[85] D. C. McKay, S. Filipp, A. Mezzacapo, E. Magesan, J. M. Chow, and J. M. Gambetta, Universal Gate for Fixed-Frequency Qubits via a Tunable Bus, Phys. Rev. Appl. **6**, 064007 (2016).

[86] M. Ganzhorn, G. Salis, D. J. Egger, A. Fuhrer, M. Mergenthaler, C. Müller, P. Müller, S. Paredes, M. Pechal *et al.*, Benchmarking the noise sensitivity of different parametric two-qubit gates in a single superconducting quantum computing platform, Phys. Rev. Res. **2**, 033447 (2020).

[87] M. Ganzhorn, D. J. Egger, P. Barkoutsos, P. Ollitrault, G. Salis, N. Moll, M. Roth, A. Fuhrer, P. Mueller *et al.*, Gate-Efficient Simulation of Molecular Eigenstates on a Quantum Computer, Phys. Rev. Appl. **11**, 044092 (2019).

[88] C. D. B. Bentley, H. Ball, M. J. Biercuk, A. R. R. Carvalho, M. R. Hush, and H. J. Slatyer, Numeric optimization for configurable, parallel, error-robust entangling gates in large ion registers, Adv. Quantum Technol. **3**, 2000044 (2020).

[89] S. Jandura and G. Pupillo, Time-optimal two- and three-qubit gates for Rydberg atoms, Quantum **6**, 712 (2022).

[90] Y. Nam, J.-S. Chen, N. C. Pisenti, K. Wright, C. Delaney, D. Maslov, K. R. Brown, S. Allen, J. M. Amini, J. Apisdorf *et al.*, Ground-state energy estimation of the water molecule on a trapped-ion quantum computer, npj Quantum Inf. **6**, 33 (2020).

[91] R. de Keijzer, O. Tse, and S. Kokkelmans, Pulse based Variational Quantum Optimal Control for hybrid quantum computing, Quantum **7**, 908 (2023).

[92] A. Wack, H. Paik, A. Javadi-Abhari, P. Jurcevic, I. Faro, J. M. Gambetta, and B. R. Johnson, Quality, speed, and scale: Three key attributes to measure the performance of near-term quantum computers, arXiv:2110.14108.

[93] M. Werninghaus, D. J. Egger, and S. Filipp, High-speed calibration and characterization of superconducting quantum processors without qubit reset, PRX Quantum **2**, 020324 (2021).

[94] G. García-Pérez, M. A.C. Rossi, B. Sokolov, F. Tacchino, P. Kl. Barkoutsos, G. Mazzola, I. Tavernelli, and S. Maniscalco, Learning to measure: Adaptive informationally complete generalized measurements for quantum algorithms, PRX Quantum **2**, 040342 (2021).

[95] L. E. Fischer, D. Miller, F. Tacchino, P. Kl. Barkoutsos, D. J. Egger, and I. Tavernelli, Ancilla-free implementation of generalized measurements for qubits embedded in a qudit space, Phys. Rev. Res. **4**, 033027 (2022).

[96] S. Sim, P. D. Johnson, and A. Aspuru-Guzik, Expressibility and entangling capability of parameterized quantum circuits for hybrid quantum-classical algorithms, Adv. Quantum Technol. **2**, 1900070 (2019).

[97] H. L. Tang, V. O. Shkolnikov, G. S. Barron, H. R. Grimsley, N. J. Mayhall, E. Barnes, and S. E. Economou, Qubit-ADAPT-VQE: An adaptive algorithm for constructing hardware-efficient ansätze on a quantum processor, PRX Quantum **2**, 020310 (2021).

[98] J. Romero, R. Babbush, J. R McClean, C. Hempel, P. J. Love, and A. Aspuru-Guzik, Strategies for quantum computing molecular energies using the unitary coupled cluster ansatz, Quantum Sci. Technol. **4**, 014008 (2018).

[99] See https://www.ibm.com/legal/copytrade.